



## NRC Publications Archive Archives des publications du CNRC

### **Analytical electron microscopy of carbon-rich mineral aggregates in solvent-diluted bitumen products from mined Alberta oil sands**

Couillard, Martin; Mercier, Patrick H. J.

This publication could be one of several versions: author's original, accepted manuscript or the publisher's version. / La version de cette publication peut être l'une des suivantes : la version prépublication de l'auteur, la version acceptée du manuscrit ou la version de l'éditeur.

For the publisher's version, please access the DOI link below. / Pour consulter la version de l'éditeur, utilisez le lien DOI ci-dessous.

#### **Publisher's version / Version de l'éditeur:**

<https://doi.org/10.1021/acs.energyfuels.6b00708>

*Energy & Fuels*, 30, 7, pp. 5513-5524, 2016-06-02

#### **NRC Publications Record / Notice d'Archives des publications de CNRC:**

<https://nrc-publications.canada.ca/eng/view/object/?id=f58fe631-e095-4385-a137-d555a1f0972d>

<https://publications-cnrc.canada.ca/fra/voir/objet/?id=f58fe631-e095-4385-a137-d555a1f0972d>

Access and use of this website and the material on it are subject to the Terms and Conditions set forth at

<https://nrc-publications.canada.ca/eng/copyright>

READ THESE TERMS AND CONDITIONS CAREFULLY BEFORE USING THIS WEBSITE.

L'accès à ce site Web et l'utilisation de son contenu sont assujettis aux conditions présentées dans le site

<https://publications-cnrc.canada.ca/fra/droits>

LISEZ CES CONDITIONS ATTENTIVEMENT AVANT D'UTILISER CE SITE WEB.

#### **Questions?** Contact the NRC Publications Archive team at

PublicationsArchive-ArchivesPublications@nrc-cnrc.gc.ca. If you wish to email the authors directly, please see the first page of the publication for their contact information.

**Vous avez des questions?** Nous pouvons vous aider. Pour communiquer directement avec un auteur, consultez la première page de la revue dans laquelle son article a été publié afin de trouver ses coordonnées. Si vous n'arrivez pas à les repérer, communiquez avec nous à PublicationsArchive-ArchivesPublications@nrc-cnrc.gc.ca.



# Analytical Electron Microscopy of Carbon-Rich Mineral Aggregates in Solvent-Diluted Bitumen Products from Mined Alberta Oil Sands

Martin Couillard and Patrick H. J. Mercier\*

Energy, Mining and Environment Portfolio, National Research Council Canada, 1200 Montreal Road, Ottawa, Ontario, Canada K1A 0R6

**ABSTRACT:** Contaminant solids in solvent-diluted bitumen product obtained by solvent extraction and solids agglomeration (SESA) of Alberta oil sands are characterized using aberration-corrected scanning transmission electron microscopy (STEM). In particular, the distribution of carbon present in these contaminant solids is determined from spatially resolved spectroscopy. Three distinct types of carbon-rich particles are identified and consist of carbonate minerals, micrometer-sized particles of toluene-insoluble organic carbon, and clay aggregates containing toluene-insoluble organic carbon. Energy-dispersive X-ray spectroscopy (EDX) maps confirm the presence of carbonates, in addition to other minerals, whose abundances are determined by a recently developed quantitative phase analysis methodology. Carbonaceous micrometer-sized particles with detectable amounts of oxygen and sulfur also appear in the elemental maps and suggest the presence of bitumen-unrelated organic materials. Finally, EDX maps also suggest an intricate sub-micrometer association of carbon with clay minerals. To map the distribution of light elements and transition metals in these clay aggregates, electron energy-loss spectroscopy (EELS) analysis has been carried out at the nanometer scale. In addition to carbon-rich regions, sub-10-nm titanium and iron oxide particles are often found dispersed on the clay surfaces. By observing clay platelets in orientations both parallel and perpendicular to the electron beam, EELS maps confirm that the carbon is present on the surface of the clays, rather than intercalated between individual clay mineral layers within the crystal structure. Furthermore, the organic coating is not uniform, displaying carbon-rich features with dimension on the order of a few nanometers, while leaving some regions of the clay mineral surface exposed. Partial nanometer-scale organic coverage has been proposed to result in a biwetttable character for clay platelets that will influence the bitumen extraction process, and such coverage has been shown here directly for the first time using spatially resolved spectroscopic microscopy observations.

## 1. INTRODUCTION

Oil sands consist of sand, clay, water, and minor amounts of other minerals (e.g., carbonates, pyrite, and titanium oxides) mixed with bitumen, which is a dense and viscous form of petroleum.<sup>1,2</sup> Under ambient conditions, bitumen does not flow and has a density similar to water. This presents significant challenges for the extraction of the bitumen, which is usually done through surface mining with water-based flotation of bitumen from the ores,<sup>3,4</sup> or through in situ methods such as the steam-assisted gravity drainage process.<sup>5</sup> As a result of the adverse environmental effects of oil sands tailings ponds,<sup>6</sup> there is recently an increasing interest in nonaqueous extraction (NAE) processes, such as solvent extraction, that do not produce wet tailings.<sup>7–11</sup> An additional challenge for any recovery processes is the presence of microaggregated minerals and water in the bitumen products that may eventually lead to corrosion and fouling problems in downstream upgrading operations.<sup>12</sup>

Phyllosilicate clays are problematic in many aspects of aqueous separation of bitumen from oil sands by flotation.<sup>13–18</sup> Clay particles may arise in bitumen products owing to the formation of water-in-oil emulsion during the extraction process,<sup>18</sup> which reduces the recovery of bitumen and increases the water content in the final bitumen product.<sup>19</sup> Adsorption of organic matter onto clay surfaces<sup>20–22</sup> may also result in a biwetttable character for the platelets, and an emulsion can then be stabilized by an accumulation of these platelets at the bitumen–water interface.<sup>23</sup> The extent to which bitumen

droplets are covered by fine particles is commonly referred to as slime coating.<sup>19</sup> Through carryover (entrainment), other types of solids may also report to the bitumen products, such as soluble salts. Zircon and titanium-bearing minerals are known to float to the bitumen froth.<sup>17</sup> Naturally oleophilic or hydrophobic minerals, for instance iron oxides, have also been found in solvent-diluted bitumen products from solvent extraction of Alberta oil sands.<sup>24,25</sup>

The carbon present in contaminant solids within coker-feed bitumen from oil sands operations has previously been assigned to aromatic polar organic matter derived from humic and asphaltene-like substances.<sup>23,26</sup> These studies were based on surface science analytical tools such as X-ray photoelectron spectroscopy (XPS), Fourier transform infrared spectroscopy (FTIR), and time-of-flight secondary ion mass spectroscopy (ToF-SIMS). By simultaneously detecting inorganic and organic elements in the surface layer using ToF-SIMS, ref 26 also concluded that the surface layer of organic matter is patchy, rather than continuous. This analysis is consistent with the biwetttable characteristics previously observed for clays.<sup>27</sup> Synchrotron-based techniques have also been applied to study the clay–organic interaction.<sup>28</sup> In particular, X-ray absorption spectroscopy (XAS), acquired in a scanning transmission X-ray

Received: March 28, 2016

Revised: May 26, 2016

Published: June 2, 2016

microscopy (STXM) mode,<sup>29,30</sup> has been performed on carbon-rich regions of clay mineral particles extracted from oil sands, and the bound organics were identified as being primarily aromatic.<sup>31</sup>

To further characterize clay–organic complexes present in solvent-diluted bitumen products, there is a need for spatially resolved analysis of the carbon at the nanometer scale. Transmission electron microscopy (TEM) is known to provide such analysis with sufficient resolution and has previously been applied to the study of contaminant solids in oil sands bitumen products.<sup>32–34</sup> In particular, scanning transmission electron microscopy (STEM), coupled with energy-dispersive X-ray spectroscopy (EDX) and electron energy-loss spectroscopy (EELS), can be combined to provide both structural and chemical analysis. EDX can detect a wide range of elements and provide maps that are complementary to bulk elemental analysis with X-ray fluorescence (XRF) spectrometry. Similarly, mineral association between the various phases identified by bulk X-ray diffraction (XRD) analysis can also be directly visualized by STEM-EDX. Since clays are radiation sensitive, the resolution of chemical maps will be dose-limited. EELS has a significantly higher collection efficiency than EDX and is also more sensitive to light elements, and it is therefore ideally suited to study organoclay aggregates.<sup>35–37</sup>

In this work, we study the carbon distribution within residual solids found in solvent-diluted bitumen product obtained by laboratory-scale solvent extraction and solids agglomeration of Alberta oil sands.<sup>38</sup> In particular, the clay–organic aggregates are analyzed at nanometer scale with EELS. The solids present in the solvent-diluted bitumen product are isolated from the sample using a toluene–water interfacial separation technique described below. Three major sources of carbon are identified in the residual solids. (1) *Carbonate minerals* (siderite in crystalline form is identified by XRD, and particles of other carbonate minerals (dolomite, calcite, and/or ankerite) are also directly imaged in EDX); (2) *micrometer-sized carbon-rich particles* (carbonaceous particles, also containing oxygen and sulfur, appear in elemental maps as irregular micrometer-sized features); (3) *organic carbon intermixed with clay* (EELS analysis of clay mineral platelets provides evidence of a nonuniform coating, with carbon-rich features of only a few nanometers).

## 2. EXPERIMENTAL SECTION

### 2.1. Materials (Oil Sand Samples and Separation Process).

The residual contaminant solids characterized in this work were obtained from solvent-diluted bitumen produced by laboratory-scale solvent extraction and solids agglomeration (SESA) of Alberta oil sands.<sup>38</sup> The SESA experiment performed to produce the bitumen product was carried out using cyclohexane as the solvent. Deionized water was added for agglomeration in order to achieve a nominal water-to-mineral-solids mass ratio of 0.12 during agglomeration. The total amount of solids (i.e., the mass concentration of solids in weight percent) present in the solvent-diluted bitumen product from the SESA experiment was not determined. Nonetheless, a settled solids layer accumulated to the bottom of the laboratory-scale SESA bitumen product after prolonged standing in a 2 L glass jar. The solids fractions analyzed here were isolated from those settled solids using the following toluene–water interfacial separation technique: (1) The settled solids at the bottom of the 2 L jar were scraped off (approximately 2 g) and placed in a 100 mL “jar A”. (2) A 10 g amount of water was added to jar A and the remainder filled with toluene. (3) Jar A was agitated vigorously for 5 min using a high-intensity Spex mixer and then centrifuged for 20 min at 950 gravities. (4) The toluene supernatant was removed and discarded. (5) Steps 3 and 4 were repeated with fresh toluene until the supernatant was clear

and colorless. (6) Jar A was three-quarters filled with water and the remaining filled with toluene. This was hand shaken and left to sit for a minimum of 20 min. (7) Following this previous step, two layers formed in jar A: (i) a cloudy water layer showing the presence of hydrophilic solids (HPS) and (ii) a layer of “organic-rich solids” (ORS) accumulated at the toluene–water interface. The ORS layer was removed with a spatula and placed into a separate 100 mL “jar B”. (8) Steps 6 and 7 were repeated until there was no more ORS material remaining in the initial jar A. (9) Jar B was half-filled with water and half with toluene, was hand shaken, and then allowed to sit for 20 min. (10) There was still some cloudiness, so this water layer was transferred out of the jar. (11) Steps 9 and 10 were repeated until there was no cloudiness in jar B. (12) Jars A and B were placed in an oven at 110 °C overnight.

**2.2. Analytical Methods.** Bulk analyses of the chemical and mineralogical composition of solids in the ORS fraction were obtained as follows. Absolute concentrations for elements heavier than Na were measured with commercial equipment for X-ray fluorescence (XRF) elemental analysis (Bruker AXS S4 Pioneer XRF spectrometer) following the calibration protocol described in ref 39, standard equipment (Elementar vario EL cube) was used for measuring absolute total contents of carbon and sulfur in the sample. Commercial equipment for XRD profile collection (Bruker AXS D8 Advance system  $\theta$ – $\theta$  powder diffractometer) and Rietveld analysis with TOPAS 5.1 (Bruker AXS, Karlsruhe, Germany) were used to determine abundance ratios for the crystalline mineral phases. The mineralogical compositions of selected samples were obtained using a new quantitative phase analysis (QPA) methodology parametrized with singular-value decomposition (SVD) based least-squares refinement. This novel methodology, referred to as SVD-QPA,<sup>40,41</sup> extends standard QPA from a maximum of 6–10 phases to a generalized methodology capable of treating an unlimited number of phases, including both crystalline (mineral, inorganic) and amorphous (organic, nanoparticle) phases. The SVD-QPA methodology employs a linear least-squares refinement procedure to determine mineralogical compositions based on combined experimental results from metal concentrations by XRF (Si, Al, K, Mg, Fe, Ti, Zr, Mg, Ca, and P), carbon and sulfur contents, and mineral ratios determined by Rietveld analysis of XRD powder patterns.

Imaging of the residual mineral solids was carried out using both scanning electron microscopy (SEM) and transmission electron microscopy (TEM). The SEM was carried out using a JEOL 840A microscope. The powdered samples were first encapsulated in a polymerized resin and polished mechanically to obtain a flat surface topography. TEM specimens were prepared by first dispersing the solid powder in ethanol and then sonicating for 15 min. One drop of the solution was then placed onto a 200 mesh TEM copper grid coated with a lacey carbon support film (Ted Pella) and dried in air. A FEI Titan<sup>3</sup> 80–300 TEM operated at 300 keV and equipped with a CEOS aberration corrector for the probe forming lens and a monochromated field-emission gun was used to acquire both high-resolution TEM (HRTEM) and annular dark-field (ADF) images. ADF images were collected using a high-angle annular dark-field (HAADF) Fischione detector in STEM mode. This technique provides signal intensity related mainly to the atomic number ( $Z$ ) and the thickness of the region analyzed. When combined with an aberration corrector, ADF-STEM can reach a sub-angstrom resolution<sup>42</sup> and single-atom sensitivity.<sup>43</sup>

The TEM instrument is also equipped with an EDX spectrometer (EDAX Analyzer, DPP-II) and an EELS instrument. The EELS analysis was performed on a Gatan Tridiem 866 image filter, which includes a CCD camera that was also used for the bright-field TEM and HRTEM imaging. To obtain elemental maps, spatially resolved EELS and EDX were collected in STEM. To optimize the signal intensity, EDX spectra were acquired with the specimen tilted at 15°. In general, EDX is more sensitive to heavier elements, while EELS is more sensitive to light elements. EELS is therefore better suited to map the carbon distribution at high-spatial resolution on clay surfaces and at the interface with minerals. Chemical maps are extracted from spectrum images, which consist of a two-dimensional image with a full

EDX or EELS spectrum acquired at each pixel. The ADF signal is also collected simultaneously with the spectroscopy signal. The elemental maps are then obtained by integrating peaks in EDX and edges in EELS following a background subtraction.<sup>44</sup>

### 3. RESULTS AND DISCUSSION

The analysis of the contaminant solids separated from the solvent-diluted bitumen product is performed in two steps. First, a bulk characterization quantifies the overall elemental composition and mineral content of the contaminant solids. The second step in the analysis consists of a spatially resolved characterization. By combining both SEM and TEM, we image mineral solid particles from the millimeter scale down to the atomic scale. EDX spectrum imaging provides evidence of association between the minerals identified by bulk XRD analysis, and nanometer-scale EELS analysis is carried out to map the carbon distribution.

**3.1. Bulk Composition and Mineralogy.** Table 1 summarizes the elemental analysis for the two solids fractions,

**Table 1. Elemental Composition in Weight Percent for the Organic-Rich Solids (ORS) and the Hydrophilic Solids (HPS)<sup>a</sup>**

elements	composition (wt %)	
	ORS	HPS
C	12.35	2.29
S	6.06	1.23
Si	10.26	31.97
Al	6.32	6.93
K	1.01	1.19
Fe	17.39	1.0
Ti	2.05	0.32
Ca	0.94	0.68
Mg	0.55	0.48
P	0.23	0.04

<sup>a</sup>See text for description.

HPS and ORS, isolated from the solvent-diluted bitumen product using the toluene–water interfacial separation technique described above. The ORS fraction is hydrophobic, and accumulates at the toluene–water interface, whereas the HPS fraction comprises the solids partitioning to the water layer. The measurements reveal a significantly higher carbon content for the ORS fraction, estimated at 12.3 compared to 2.3 wt % for the HPS fraction. The natural hydrophilicity of quartz may partially explain the larger content of silicon in the HPS fraction. Clay minerals are found in both fractions, as suggested by the Al content (as well as K content for illite). This observation is consistent with a biwettable character for the organoclay microaggregates present in the bitumen product. Finally, iron and, to a lesser extent, titanium both represent a significant fraction of the elements present in the ORS fraction.

Mineral quantification results for the ORS fraction are summarized in Table 2. These results were obtained with the SVD-QPA methodology described above by combining (i) mineral ratios determined by Rietveld analysis of the XRD powder profile in Figure 1 and (ii) elemental analyses reported in Table 1. Table 2 also lists the abbreviations and chemical formulas of the 19 mineral and three amorphous phases considered for quantitative phase analysis. The least-squares SVD-QPA methodology was used to determine mineralogical

composition of the ORS sample based on a least-squares SVD-QPA model including these 22 phases.

The mineralogical composition results (Table 2) confirm the presence of a large fraction of clay minerals, with kaolinite (KAO) and illite (ILL) as the two prevalent phyllosilicate phases. Even if naturally hydrophilic, quartz (QTZ) and amorphous silica (SIL) are also found in the ORS fraction, possibly due to modification of their surfaces, by association with other minerals or through entrainment. By and large, iron is the most abundant element among those analyzed (Table 1) and it can be found mainly as pyrite (PYR), siderite (SID), and amorphous iron oxide–hydroxide phases (AFE) (Table 2). Note that the AFE phase assumed in the SVD-QPA model was not directly observable by XRD. Figure 1 clearly shows that pyrite and siderite are the two main crystalline phases contributing to the XRD powder pattern. In addition to siderite, other carbonate phases such as dolomite (DOL), calcite (CAL), and ankerite (ANK) explain part of the carbon content detected in the sample. Ti-bearing minerals, in particular rutile (RUT) and anatase (ANA), are also detected by XRD. The mineralogical composition results account for around 92 wt % of the total mass of the ORS fraction.

**3.2. Electron Microscopy Imaging.** SEM images presented in Figure 2 clearly show the heterogeneity of the sample. The brightest features correspond to minerals bearing heavy elements such as Fe or Ti. In particular, cube particles are commonly observed (arrow 1) and are identified as pyrite. Darker areas (e.g., arrow 2) include mineral matrices largely composed of aluminosilicates and appear heterogeneous even at the micrometer scale. Other minerals are expected to be associated with the clays in those regions.

ADF-STEM images shown in Figure 3a clearly display mineral particles with sub-micrometer dimension. Based on the contrast, which is related to the atomic number and the shape of the particles, a wide range of mineral phases are discernible. Pyrite particles appear again as strongly faceted particles. At higher resolution (Figure 3b), the pyrite particle visible near the bottom of the image appears homogeneous except near its surface. Evidence of weathering (Figure 3b, arrow), resulting in a surface layer of oxide, has been confirmed by EDX elemental profiles and explains the darker contrast observed in ADF images. In contrast, the particle located near the middle of the image appears heterogeneous. These particles consist mainly of clay minerals mixed with organic carbon, as revealed by EDX. In addition to mapping carbon, we will also demonstrate in the next section that the clay aggregates also contain metal-bearing minerals (e.g., iron or titanium oxides) that sometime appear as particles of only a few nanometers.

Clay minerals (e.g., kaolinite, illite, and chlorite) consist of stacks of basic composite layers. This layered atomic structure produces flake-like particles, which typically stand either parallel or perpendicular to the electron beam in the TEM. Higher-resolution TEM images shown in Figure 3c,d clearly show clay particles oriented in both directions. For particles lying flat on the substrate (defined here as perpendicular orientation), steps are observed, suggesting a variation in the number of constituent layers. The facets observed are consistent with the quasi-hexagonal structure of the basic composite layers of clay minerals. For particle observed with a parallel orientation (i.e., the TEM optical axis is perpendicular to the normal of the composite layers), as in Figure 3d, the individual layers can be directly imaged and counted. Phyllosilicates with only a few (one to three) layers are commonly observed. Moreover, these

Table 2. Mineralogical Composition of Residual Solids in ORS Fraction Determined by SVD-QPA Methodology

phase concentration (wt %)	abbreviation	phase	chemical formula	
QTZ + SIL	7.05 (0.14)	QTZ	quartz	SiO <sub>2</sub>
ILL	12.61 (0.02)	ILL	illite	K <sub>0.8</sub> Al <sub>2</sub> (Al <sub>0.8</sub> Si <sub>3.2</sub> )O <sub>10</sub> (OH) <sub>2</sub>
KAO	18.34 (0.64)	KAO	kaolinite	Al <sub>2</sub> Si <sub>2</sub> O <sub>5</sub> (OH) <sub>4</sub>
CHL	0.57 (1.53)	CHL	chlorite	(Mg <sub>2.5</sub> Fe <sub>2.5</sub> Al) (AlSi <sub>3</sub> )O <sub>10</sub> (OH) <sub>8</sub>
PYR	11.33 (0.02)	CAL	calcite	CaCO <sub>3</sub>
SID + AFE	23.32 (0.25)	DOL	dolomite	CaMg(CO <sub>3</sub> ) <sub>2</sub>
DOL + CAL + ANK	2.83 (0.16)	ANK	ankerite	CaFe <sub>2/3</sub> Mg <sub>1/3</sub> (CO <sub>3</sub> ) <sub>2</sub>
RUT + ANA	3.40 (0.01)	SID	siderite	FeCO <sub>3</sub>
ZIR	0.00 (0.01)	PYR	pyrite	FeS <sub>2</sub>
GYP	0.005 (0.001)	ZIR	zircon	ZrSiO <sub>4</sub>
BAS	0.005 (0.001)	RUT	rutile	TiO <sub>2</sub>
ANO	0.005(0.001)	ANA	anatase	TiO <sub>2</sub>
SAN	0.005 (0.001)	ILM	ilmenite	FeTiO <sub>3</sub>
APA	1.24 (0.01)	LEP	lepidocrocite	FeO(OH)
ORC	11.42 (0.52)	GYP	gypsum	CaSO <sub>4</sub> ·H <sub>2</sub> O
clay minerals (ILL + KAO + CHL)	31.51 (0.44)	BAS	bassanite	CaSO <sub>4</sub> ·0.5H <sub>2</sub> O
heavy minerals (SID + PYR + ZIR + RUT + ANA + ILM + LEP)	38.10 (0.24)	ANO	anorthite	CaAl <sub>2</sub> Si <sub>2</sub> O <sub>8</sub>
total mass accounted for	92.16 (0.10)	SAN	sanidine	KAlSi <sub>3</sub> O <sub>8</sub>
		APA	apatite	Ca <sub>5</sub> (PO <sub>4</sub> ) <sub>3</sub> (OH)
		ORC	amorphous organic carbon	C <sub>1.00</sub>
		SIL	amorphous silica	SiO <sub>2</sub>
		AFE	amorphous Fe oxide-hydroxide	Fe(OH) <sub>3</sub> or FeO(OH)H <sub>2</sub> O

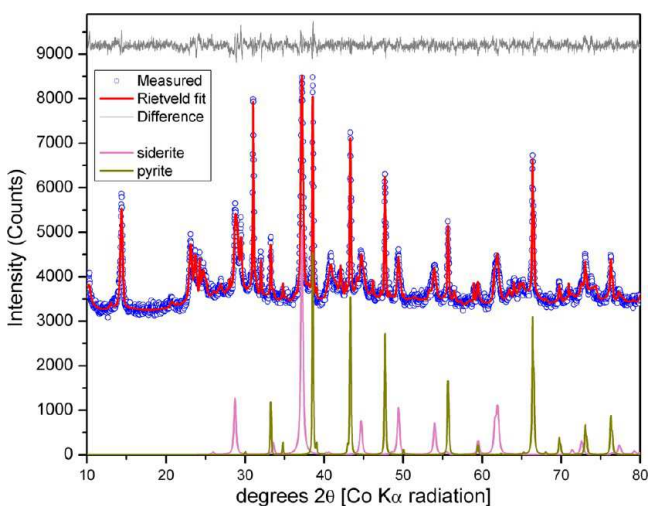


Figure 1. Rietveld analysis of XRD powder pattern measured for the ORS fraction.

minerals are also found in bundles and at the interface with other minerals.

### 3.3. Spatially Resolved Composition and Mineralogy.

**3.3.1. Overview of Mineral Particles.** Elemental mapping using EDX in STEM, as shown in Figure 4, highlights the wide variety of fine minerals present at the micrometer scale. An EDX spectrum (Figure 4b) acquired over the whole region of the corresponding image (Figure 4a) displays characteristic peaks that confirm the presence of the elements previously quantified using XRF and summarized in Table 1. Fe, Ti, and Ca peaks indicate the presence of metal bearing phases, and strong signals from Al and Si are associated mainly with clay minerals, which also include K for illite. It is important to note that some peaks are not associated with the contaminant solids studied here. In particular, spurious X-rays explain the intensity of the Cu peaks, which originate from the TEM grid, and part of the C signal is associated with the lacey-C support film. At the scale of a few micrometers, we observe significant variation in the overall composition. For this particular region, Ti displays a peak more intense than elsewhere on the specimen.

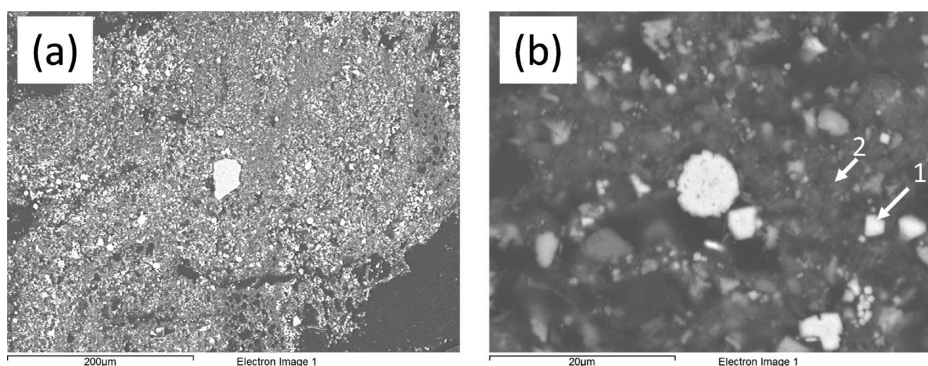
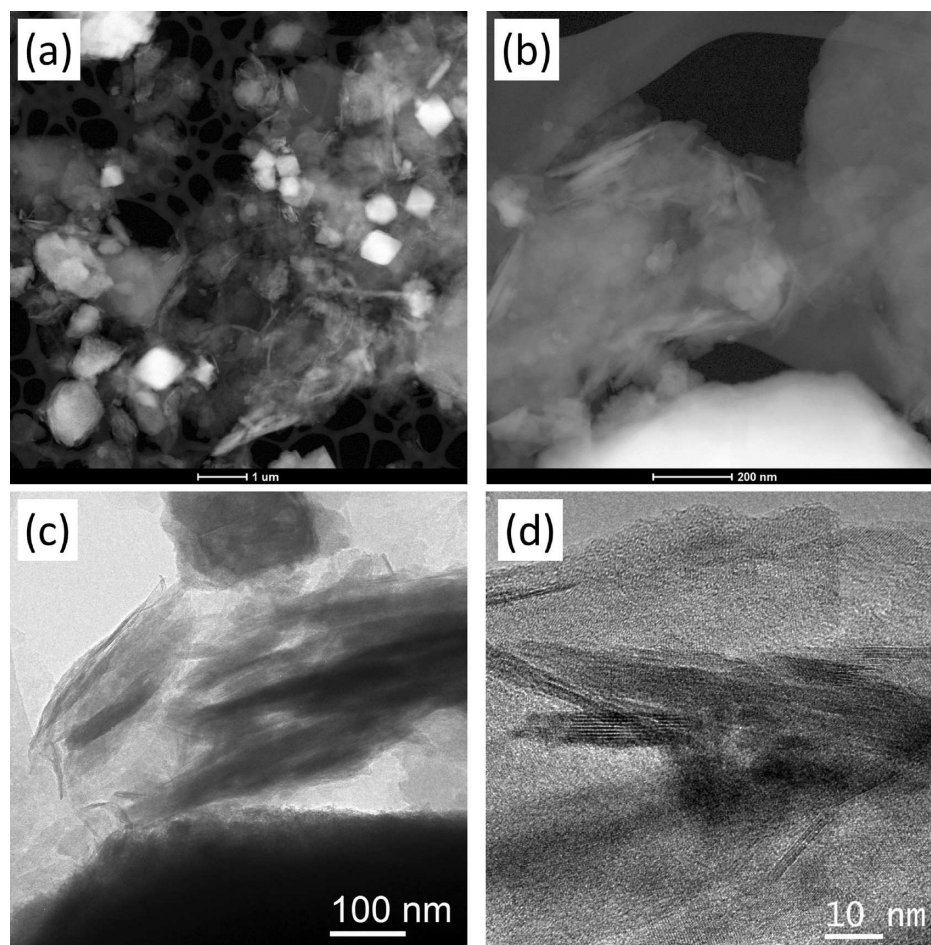


Figure 2. SEM images of the ORS fraction of the contaminant solids.



**Figure 3.** (a and b) ADF-STEM images, (c and d) high-resolution TEM images of the ORS fraction of the contaminant solids.

Figure 4c presents chemical maps extracted from the spatially resolved EDX. The maps were obtained by integrating the peak intensity for the corresponding elements. The Si signal covers most of the area shown in Figure 4a. As expected for clay minerals, it also correlates well with the Al signal, except for a few isolated particles that suggest the presence of quartz/silica particles, which is consistent with the quartz reflections measured by XRD. Sub-micrometer mineral particles containing both Ca and P, likely apatite, are detected in the EDX maps. The small dimension of these particles probably explains why their overall content is below the detection limit of the XRD analysis. Ti appears as oxide particles with various morphologies. Rutile minerals are often observed as clearly distinguishable rod-shaped particles, whereas anatase is expected to form more spherical particles. The Ti signal also overlaps in some regions with the Fe signal, suggesting the presence of ilmenite. Oxides, such as ilmenite, are only one form of Fe-bearing minerals. Other forms are expected to include oxyhydroxides, sulfides, and carbonates. For instance, pyrite particles can be clearly identified by comparing the Fe and S signal. On the elemental maps, there is also an example of an iron-bearing carbonate such as siderite. For several particles, the signals of Fe, Mg, and Ca overlap in regions where a C signal is also detected. These particles are consistent with the presence of a mixture of carbonate phases such as calcite, dolomite, and/or ankerite, which are identified as small diffraction peaks in the XRD pattern.

**3.3.2. Carbon Distribution at the Micrometer Scale.** The C map shown in Figure 4c renders the lacey carbon support clearly visible. This support consists of an irregular mesh of micrometer-sized holes. Thus, a reliable measurement of C content in minerals can only be obtained when the electron probe is positioned over one of those holes. The carbon distribution also clearly reveals irregular micrometer-sized particles. For these particles, the C signal is significantly more intense than the signals from the lacey support film or the surrounding carbonate minerals. When the STEM probe was positioned over these carbon-rich particles, the convergent beam electron diffraction did not display reflections, which indicates that these particles are amorphous. These carbon-rich particles are therefore not expected to produce any crystalline reflections in the XRD pattern. This observation is consistent with assuming the presence of an amorphous organic carbon phase (ORC) in the SVD-QPA model used to determine the overall mineralogical composition of the sample (Table 2). O and S maps also display detectable signals in the same C-rich regions where those particles appear, which may also contain H and N, but EDX cannot confirm the presence of these elements because it does not detect the first and is less sensitive to the second. We attribute these micrometer-sized carbon-rich particles to the presence of a form of toluene-insoluble organic carbon such as kerogen or coal; the occurrence of such a type of bitumen-unrelated organic matter in oil sands has been described previously.<sup>45</sup> Finally, C also appears in several regions as a diffuse signal that extends over the holes in the support. As

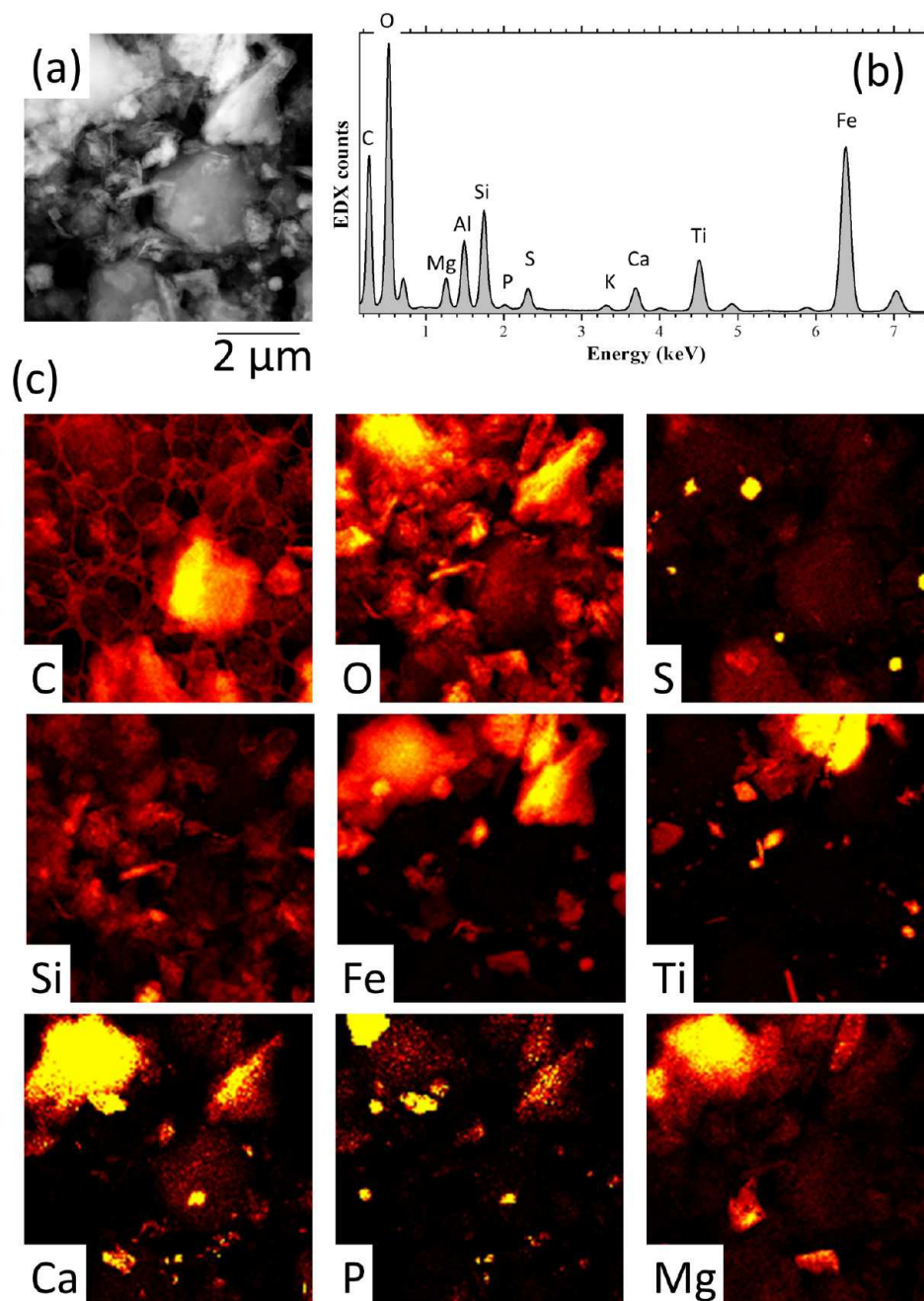


**Figure 4.** (a) ADF-STEM image of the ORS fraction, (b) EDX spectrum summed over the whole region shown in panel a, and (c) EDX elemental maps.

discussed below, a carbon signal associated with particles containing mainly clay minerals is detected and is expected to be a major component of the overall carbon content associated with the contaminant solids studied here.

To confirm the various origins of the carbon signal, Figure 5 presents a series of spatially resolved EDX spectra (Figure 5b) extracted at the specific locations labeled in the image (Figure 5a). The colored chemical map in Figure 5a is composed of three elemental maps from Figure 4, where red, green, and blue correspond to C, Si, and Fe, respectively. This figure illustrates the distribution of metal-bearing minerals and toluene-insoluble organic carbon particles in a matrix of clay minerals. Some regions analyzed do not include a detectable amount of carbon. For instance, spectrum 1 shows a Fe–Ti–O particle (presumably ilmenite) where the C peak is absent. In this

region, the C signal is not considered significant. In contrast, a carbonate mineral, identified as ankerite and containing Fe–Ca–Mg along with O and C, is found in region 2 and has a corresponding spectrum clearly displaying a C peak. The most intense C peaks are detected at the toluene-insoluble organic carbon particle locations. Spectrum 3 shows this dominant C contribution, along with a smaller O signal. Other peaks on this spectrum can be associated with the surrounding minerals, but a clear increase in S is systematically observed. To a lesser extent, Ca also appears to be associated with this phase of carbon. We note that similar presence of Ca and S has been detected previously in kerogen particles using an electron microscope equipped with an EDX detector.<sup>46</sup> For a region containing clay minerals, spectrum 4 displays prominent O, Al, and Si peaks, along with a smaller K peak. Some Fe is also

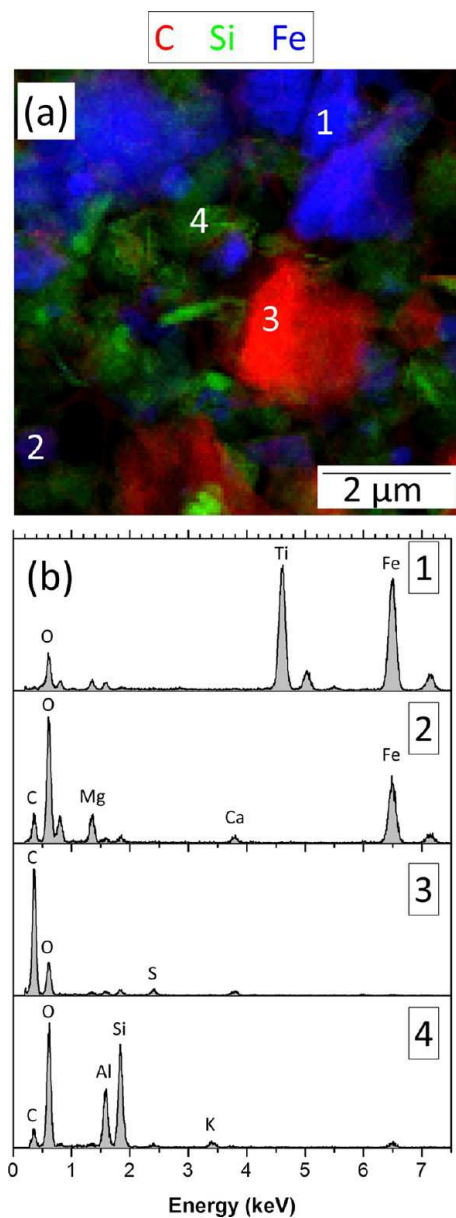


**Figure 5.** (a) EDX elemental maps for three elements (C, Si, and Fe) for the region shown in Figure 4. (b) EDX spectra taken from the regions labeled in panel a.

detected, and the signal may originate from small particles on the clay surfaces. Iron oxide and titanium oxide sub-micrometer particles often appear scattered randomly on the clay surfaces (examples are given below). In these regions, the C signal remains clearly visible. The EDX observation therefore suggests an intermixing of C with clay on a fine sub-100-nm scale.

It is important to emphasize that the overall composition varies considerably at the micrometer scale. For instance, ilmenite and ankerite minerals represent a significant fraction of the minerals observed in Figure 4, but overall, as determined by the SVD-QPA analysis (Table 2), they represent a small proportion of the residual solids associated with the ORS fraction. Similarly, the toluene-insoluble organic carbon particles do not systematically appear on micrometer-scale images. Clay minerals, in contrast, cover most of the TEM specimen examined. Thus, the organic carbon associated with

clays is expected to represent a significant fraction of the overall toluene-insoluble organic carbon content.

**3.3.3. Carbon Distribution at the Nanometer Scale.** Mapping the carbon distribution associated with clay mineral particles is performed at the nanometer scale using EELS spectrum imaging. Figure 6 presents an ADF-STEM image along with a composite image of three EELS elemental maps. Red, green, and blue correspond to C, Fe, and O, respectively. The central feature on the image is an aggregate of thin clay platelets lying almost parallel to the electron beam. It is similar to the clay bundle observed in HRTEM (Figure 3d) where some delaminated flakes can have a width of only a few composite phyllosilicate layers. On each side of the aggregate, other clay mineral particles can be observed with an orientation almost perpendicular to the beam, but with regions ~10–50 nm in lateral extension that have much brighter contrast and suggest some heterogeneity. The elemental maps reveal that, in these bright regions, small iron oxide particles have precipitated on the clay mineral surfaces. In the lower half of the image, a large C-rich feature, with a diameter around 600 nm, is another example of a toluene-insoluble organic carbon particle similar to the ones identified in the EDX analysis.

The C and O maps shown in Figure 6 also clearly demonstrate the association of carbon with clay minerals. The variations in O and C signal (Figure 6b) observed in the aggregate near the center of the image suggest that C accumulates at the surface of the thin clay platelets. Within the bundle, darker areas on the ADF-STEM image (Figure 6a) represent regions without clay minerals. The carbon map displays a signal in the same regions, highlighting the fine intermixing of clay minerals and organic matter. Overall, the carbon intensity in Figure 6b follows the contour of the parallel platelets in Figure 6a. In addition, the O and C signals do not significantly overlap within this clay bundle. Both of these observations indicate that the carbon is on the surface of the clays rather than incorporated in their crystal lattice. When clay platelets are viewed along a direction perpendicular to the electron beam, such as in regions 1 and 2 (Figure 6b), the C content is also shown to vary considerably. For the more inhomogeneous region on the left (Figure 6b), which appears to consist of multiple smaller particles, the C signal often mimics the nanometer-scale features observed on the ADF-STEM image (Figure 6a).

The elemental variations can be better visualized on the individual spatially resolved EELS spectra, which are shown in Figure 6c. Energy-loss spectra display edges with onsets that correspond to the minimum amount of energy loss experienced by the incident electrons due to the excitation of inner shell electrons.<sup>47</sup> The onsets are element specific, and, as discussed below, the fine structures of the edge are influenced by the chemical bonding environment. In contrast to EDX, EELS is generally limited to a chosen energy window that only includes a limited number of elements. Here, the Al, Si, C, O, and Fe signals are collected. For better visibility, the background signal was removed from the EELS spectra (raw data with the background signal are shown later for a more limited energy range). Core-loss edges sometimes overlap, as it is the case for Al and Si. As can be seen in the spectra, the Al edge extends into the energy region of the Si edge. Well separated elements, such as C, O, and Fe, produce signals that are easier to extract into chemical maps.

For the three spectra displayed in Figure 6c, corresponding to regions 1, 2, and 3 labeled on the chemical maps (Figure 6b),

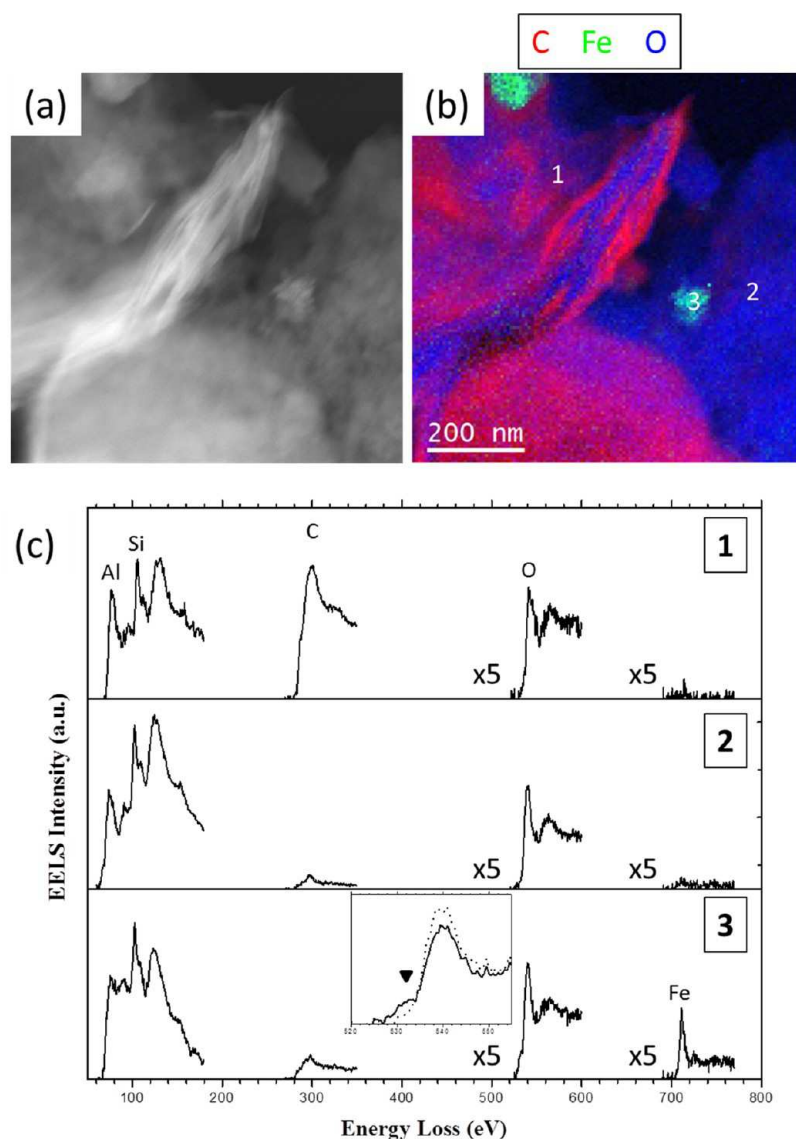


**Figure 6.** (a) High-resolution ADF-STEM image of a clay particle in the ORS fraction and (b) EELS elemental maps for three elements (C, Fe, and O). (c) Energy-loss spectra for the regions labeled in panel b. The inset for spectrum 3 shows the O K-edge fine structures for region 3 (full line) and region 2 (dotted line).

the Al, Si, and O ratio appears fairly constant. In contrast, the C and Fe signals display strong variations. The region (spectrum 1) on the top left has a higher carbon content than the two other regions on the bottom right (spectra 2 and 3). However, even if not clearly visible on the chemical map, the more homogeneous region on the right also displays a carbon edge on the spectrum. Interestingly, the carbon signal increases in the vicinity of the iron-bearing particle, as shown in spectra 3. From the Z contrast signal of the ADF-STEM image, it is clear that both regions (1 and 2) are heterogeneous and do not consist solely of individual flat clay platelets.

**3.3.4. Carbon Coating of Clay Platelets.** For a closer view of the carbon distribution on clay surfaces, Figure 7 presents chemical maps for a region with clearly distinguishable clay platelets. The thickness of the platelets increases from the top left to the bottom right. The Z contrast of the ADF image is not completely uniform, in particular for the bottom right region, and it also displays sub-10-nm features. EELS elemental maps shown in Figure 7b reveal that these features correspond to titanium oxide nanoparticles, precipitated on the clay surface. C

is also observed to accumulate preferentially at the edges of the platelets, producing for instance a thin diagonal line on the chemical maps. On individual clay platelets, for the three regions of varying thickness, the carbon coverage can be described as patchy rather than continuous. The variations appear clearly on the spectra presented in Figure 7c, for the regions labeled in Figure 7b. In this image (Figure 7c), the raw spectra with the background signal are displayed, and the C, Ti and O edges are observed in the selected range of energy loss. The Ti signal is highly localized (spectrum 3) and may be correlated with a slight increase in carbon, as previously observed for iron oxide nanoparticles. Between regions 1 and 2, separated by only  $\sim 10$  nm, the carbon signal rapidly decreases to below the detection limit. This indicates that sections of the clay surfaces are not covered by toluene-insoluble organic carbon and remain exposed.

As displayed on intensity profiles for the same region (Figure 8), the O signal increases in a stepwise fashion for increasing clay platelet thickness, whereas the C signal produces more localized features of similar intensities. Overall, more carbon-

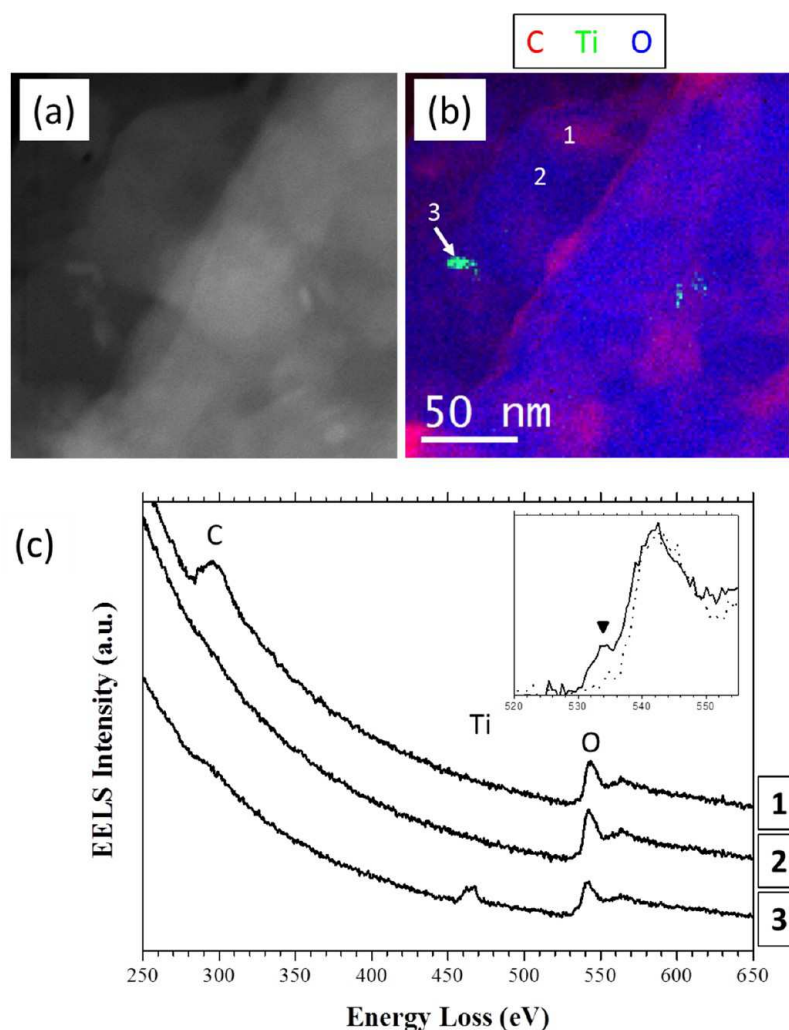


**Figure 7.** (a) High-resolution ADF-STEM image of a clay particle in the ORS fraction and (b) EELS elemental maps for three elements (C, Ti, and O). (c) Energy-loss spectra for the regions labeled in panel b. The inset in panel c shows the O K-edge fine structures for region 3 (full line) and region 2 (dotted line).

rich features are observed in regions that are less homogeneous, but all of these features display a comparable EELS intensity. A signal that is independent of the platelet thickness is also consistent with carbon as a surface coating rather than incorporated within the atomic layered structure of the clay minerals.

**3.3.5. Suggested Further Work Related to the Speciation of Carbon.** In EELS, the shape of an edge following the onset also provides information on the bonding environment. For instance, O K-edges observed in Figure 6 and Figure 7 display a prepeak for Ti and Fe particles that is absent for the O K-edge associated with clays, consistent with previous studies on similar systems.<sup>35</sup> This prepeak is associated with O bonded to Fe and Ti. A preliminary analysis (not shown) of the near-edge structure in EELS spectra for C K-edge was performed with an energy resolution of 0.6 eV. Characteristics associated with carbon that would be structurally incorporated in the clay crystals, which have previously been described for carbon–clay complexes,<sup>37</sup> were not detected. Thus, our results point to carbon being absorbed on the surface of the clay. This conclusion is also supported by the two other observations described earlier, namely, that (1) the C signal intensity appears to be independent of the clay platelet thickness and that (2) the

C maps observed for clay bundles in the parallel orientation display contrast only on the surface of the clay features or in regions between delaminated platelets.

The onset of the potassium L-edge occurs at 294 eV, just 10 eV above the C K-edge. The carbon maps shown here were therefore obtained by choosing an integration window below the potassium L-edge. If both elements are present, the edges will overlap. Thus, it is easier to analyze the potassium content when no carbon is present. For the regions without C coating found in Figure 7, no potassium signal was detected. This suggests that the clay mineral is not illite. In addition, no Fe signal was detected on the clay. But because the Mg characteristic edges are located outside the energy range of the energy-loss spectra, additional analyses would be required to unambiguously identify the clay mineral. Future work will be carried out to differentiate the type of clay minerals, as well as to identify which clay minerals among illite, kaolinite, and chlorite are most likely to have an organic coating.

The functionalities of organic carbon absorbed on a surface is however difficult to ascertain with EELS, since it is expected to be particularly sensitive to the electron beam. Analytical surface science techniques such as XPS, Tof-SIMS, and FTIR have previously been used to probe the carbon functionalities for

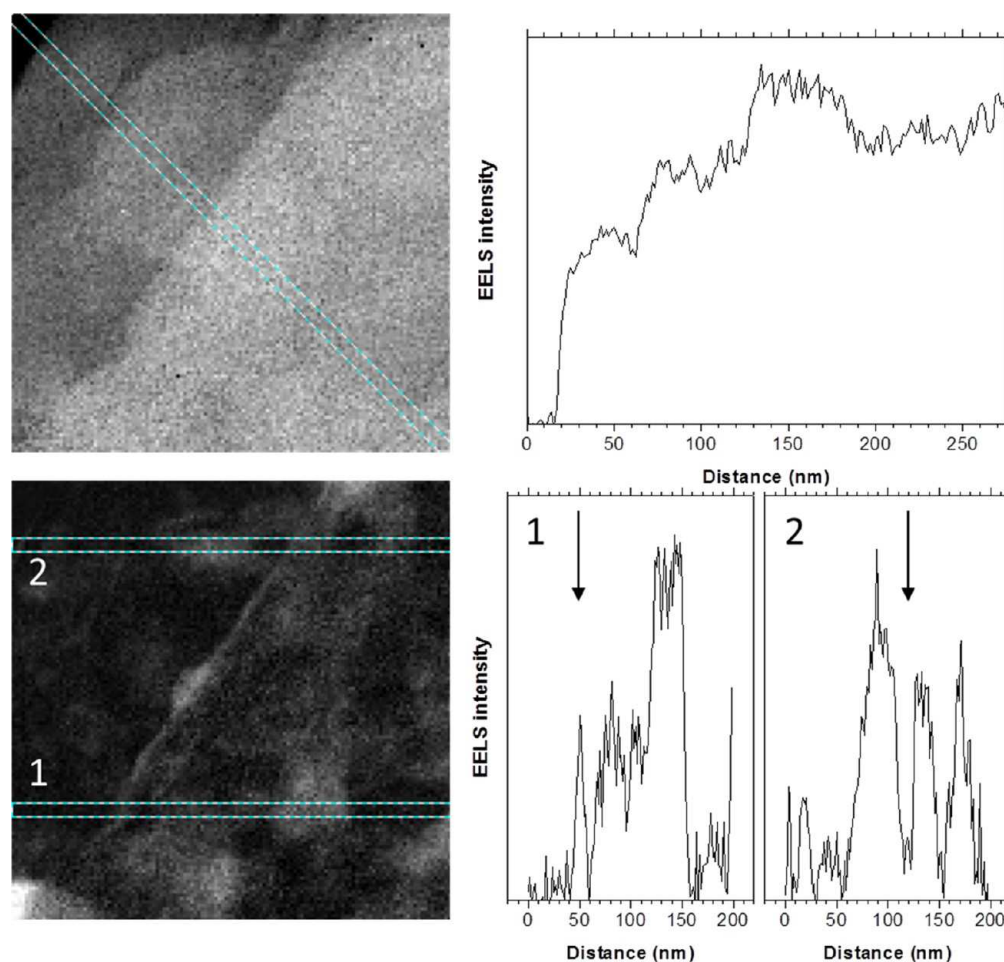


**Figure 8.** Elemental maps and intensity profiles for O (top) and C (bottom) for the region shown in Figure 7. The intensity profiles correspond to the lines labeled on the elemental maps. The two profiles for C are labeled 1 and 2 on the image, and the arrows on the intensity profiles for the C signal indicate the position of the diagonal step on the image.

organic matter that is mixed with the clay minerals. For instance, evidence of C–H, C–O, and C–OH chemical bonds were established, and clear differences were observed between marine and estuarine oil sand ores. Humic matter was identified as the main constituent of the organic matter absorbed on the clay surfaces, with some contribution from asphaltic type materials.<sup>26</sup> X-ray absorption spectroscopy (XAS), which provides near-edge structure information similar to EELS, has also been used to study the different types of organic matter mixed with clay particles.<sup>30</sup> As X-rays interact less strongly than electron with organic matter, clear spectral signatures can be observed for various carbon chemical bonding. Of particular interest for systems with a complicated mineral composition, such as the one presented here, is the ability of spatially resolved XAS in STXM to isolate individual carbon-rich clay particles.<sup>31</sup> Combining the high-energy resolution of XAS-STXM with the high-spatial resolution of EELS-STEM therefore presents a promising avenue of research on organoclay complexes.

#### 4. SUMMARY

In summary, our results combined spatially resolved chemical analysis at the nanometer and micrometer scale to resolve the carbon distribution in residual solids found in solvent-diluted bitumen product extracted from Alberta oil sands. This study focuses on the hydrophobic fraction of these residual solids,

which is found to have significantly higher carbon content. For these solids, three distinct types of carbon-rich phases are identified: carbonate minerals, micrometer-sized particles of toluene-insoluble organic carbon, and clay aggregates containing toluene-insoluble organic carbon.

Siderite, dolomite, calcite, and ankerite are four carbonate minerals detected with XRD. Elemental mapping with EDX in STEM also confirms the presence of carbonate minerals and provides information on the particle size and morphology. In contrast, the other carbon-rich phases are not crystalline and therefore do not produce clearly identified peaks in XRD. As an example, EDX mapping reveals the presence of large micrometer-sized particles, with dominant carbon content and with detectable amounts of oxygen and sulfur. These observations are attributed to the presence of toluene-insoluble organic carbon.

The intermixing of toluene-insoluble organic carbon with clay minerals, suggested by both the present EDX analysis and previous surface science studies, occurs on a fine sub-micrometer scale. To directly visualize the carbon distribution in clay–organic matter aggregates, spatially resolved EELS is employed because of its high collection efficiency and its high sensitivity to light elements. Carbon maps are obtained with a nanometer resolution for clay platelets with orientations parallel and perpendicular to the electron beam. These observations directly point to carbon being present on the surface of clay

platelets, rather than incorporated in their crystal lattice. The coating of toluene-insoluble organic carbon is observed to be nonuniform with nanometer-scale carbon-rich features. Some regions of the clay surfaces remain exposed. As clays are among the most common minerals present in the residual solids separated from the bitumen product, as confirmed by quantitative phase analysis of the mineralogical composition, surficial organic carbon is thus expected to represent a significant fraction of the overall carbon content. Clay platelets with surfaces partially covered with organic matter are expected to display a biwettable character, which will have a direct impact on the bitumen extraction process.

## AUTHOR INFORMATION

### Corresponding Author

\*E-mail: [patrick.mercier@nrc-cnrc.gc.ca](mailto:patrick.mercier@nrc-cnrc.gc.ca).

### Notes

The authors declare no competing financial interest.

## ACKNOWLEDGMENTS

We thank the Institute for Oil Sands Innovation (IOSI) at the University of Alberta for funding this project and for collaborative support through consultation and sample supply. Andre Zborowski performed the laboratory-scale SESA experiment which provided the solvent-diluted bitumen product. Daniel Tyo separated the residual contaminant solids analyzed (ORS fraction) from the SESA bitumen product. The XRF/XRD measurements were done by Bussaraporn Patarachao, and the SEM imaging was carried out by David Kingston.

## REFERENCES

- (1) Takamura, K. *Can. J. Chem. Eng.* **1982**, *60*, 538–545.
- (2) Gray, M.; Xu, Z.; Masliyah, J. *Phys. Today* **2009**, *62*, 31–35.
- (3) Masliyah, J.; Zhou, Z.; Xu, Z.; Czarnecki, J.; Hamza, H. *Can. J. Chem. Eng.* **2004**, *82*, 628–654.
- (4) Shaw, R. C.; Schramm, L. L.; Czarnecki, J. *Suspensions in the Hot Water Flotation Process for Canadian Oil Sands. Suspensions: Fundamentals and Applications in the Petroleum Industry*; Advances in Chemistry Series 251; American Chemical Society: Washington, DC, USA, 1996; Chapter 13, pp 639–656, DOI: [10.1021/ba-1996-0251.ch013](https://doi.org/10.1021/ba-1996-0251.ch013).
- (5) *Oil Sands Technology Roadmap, Unlocking the Potential*; Alberta Chamber of Resources: Edmonton, Alberta, Canada, 2004.
- (6) Kasperski, K. L.; Mikula, R. J. *Waste Streams of Mined Oil Sands: Characteristics and Remediation. Elements* **2011**, *7*, 387–392.
- (7) Nikakhtari, H.; Vagi, L.; Choi, P.; Liu, Q.; Gray, M. R. *Solvent screening for non-aqueous extraction of Alberta oil sands. Can. J. Chem. Eng.* **2013**, *91*, 1153–1160.
- (8) Hooshier, A.; Uhlík, P.; Liu, Q.; Etsell, T. H.; Ivey, D. G. *Clay minerals in nonaqueous extraction of bitumen from Alberta oil sands Part 1. Nonaqueous extraction procedure. Fuel Process. Technol.* **2012**, *94*, 80–85.
- (9) Li, X.; He, L.; Wu, G.; Sun, W.; Li, H.; Sui, H. *Operational parameters, evaluation methods, and fundamental mechanisms: Aspects of nonaqueous extraction of bitumen from oil sands. Energy Fuels* **2012**, *26*, 3553–3563.
- (10) Wu, J.; Dabros, T. *Process for solvent extraction of bitumen from oil sand. Energy Fuels* **2012**, *26*, 1002–1008.
- (11) Yu, K.; Wang, Z.; Jin, Y.; Sun, Z.; Liu, Y.; Yang, J.; Cai, Y. *Single- and multi-stage counter-current solvent extractions of bitumen from Xinjiang oil sand. Energy Fuels* **2013**, *27*, 6491–6500.
- (12) Kotlyar, L. S.; Sparks, B. D.; Woods, J. R.; Chung, K. H. *Energy Fuels* **1999**, *13*, 346–350.
- (13) Omotoso, O. E.; Mikula, R. J. *Appl. Clay Sci.* **2004**, *25*, 37–47.
- (14) Wallace, D.; Tipman, R.; Komishke, B.; Wallwork, V.; Perkins, E. *Can. J. Chem. Eng.* **2004**, *82*, 667–677.
- (15) Osacky, M.; Geramian, M.; Liu, Q.; Ivey, D. G.; Etsell, T. H. *Energy Fuels* **2014**, *28*, 934–944.
- (16) Mercier, P. H. J.; Patarachao, B.; Kung, J.; Kingston, D. M.; Woods, J. R.; Sparks, B. D.; Kotlyar, L. S.; Ng, S.; Moran, K.; McCracken, T. *Energy Fuels* **2008**, *22*, 3174–3193.
- (17) Kaminsky, H. A. W.; Etsell, T. H.; Ivey, D. G.; Omotoso, O. *Can. J. Chem. Eng.* **2009**, *87*, 85–93.
- (18) Jiang, T. M.; Hirasaki, G. J.; Miller, C. A.; Ng, S. *Effects of clay wettability and process variables on separation of diluted bitumen emulsion. Energy Fuels* **2011**, *25*, 545–554.
- (19) Bakhtari, M. T.; Harbottle, D.; Curran, M.; Ng, S.; Spence, J.; Siy, R.; Liu, Q.; Masliyah, J.; Xu, Z. *Role of Caustic Addition in Bitumen–Clay Interactions. Energy Fuels* **2015**, *29*, 58–69.
- (20) Adegoroye, A.; Wang, L.; Omotoso, O.; Xu, Z.; Masliyah, J. *Characterization of organic-coated solids isolated from different oil sands. Can. J. Chem. Eng.* **2010**, *88*, 462–470.
- (21) Adegoroye, A.; Uhlík, P.; Omotoso, O.; Xu, Z.; Masliyah, J. *A Comprehensive Analysis of Organic Matter Removal from Clay-Sized Minerals Extracted from Oil Sands Using Low Temperature Ashing and Hydrogen Peroxide. Energy Fuels* **2009**, *23*, 3716–3720.
- (22) Dongbao, F.; Woods, J. R.; Kung, J.; Kingston, D. M.; Kotlyar, L. S.; Sparks, B. D.; Mercier, P. H. J.; McCracken, T.; Ng, S. *Residual organic matter associated with toluene-extracted oil sands solids and its potential role in bitumen recovery via adsorption onto clay minerals. Energy Fuels* **2010**, *24*, 2249–2256.
- (23) Sparks, B.; Kotlyar, L.; O'Carroll, J. B.; Chung, K. *J. Pet. Sci. Eng.* **2003**, *39*, 417–430.
- (24) Nikakhtari, H.; Wolf, S.; Choi, P.; Liu, Q.; Gray, M. R. *Migration of fine solids into product bitumen from solvent extraction of Alberta oilsands. Energy Fuels* **2014**, *28*, 2925–2932.
- (25) Hooshier, A.; Uhlík, P.; Ivey, D. G.; Liu, Q.; Etsell, T. H. *Clay minerals in nonaqueous extraction of bitumen from Alberta oil sands Part 2. Characterization of clay minerals. Fuel Process. Technol.* **2012**, *96*, 183–194.
- (26) Bensebaa, F.; Kotlyar, L. S.; Sparks, B. D.; Chung, K. H. *Can. J. Chem. Eng.* **2000**, *78*, 610–616.
- (27) Kotlyar, L. S.; Sparks, B. D.; Woods, J.; Raymond, S.; Le Page, Y.; Shelfantook, W. *Pet. Sci. Technol.* **1998**, *16*, 1–19.
- (28) Covelli, D.; Hernández-Cruz, D.; Haines, B. M.; Munoz, V.; Omotoso, O.; Mikula, R.; Urquhart, S. *J. Electron Spectrosc. Relat. Phenom.* **2009**, *173*, 1–6.
- (29) Jacobsen, C.; Wirick, S.; Flynn, G.; Zimba, C. *J. Microsc.* **2000**, *197*, 173–184.
- (30) Lehmann, J.; Solomon, D.; Kinyangi, J.; Dathe, L.; Wirick, S.; Jacobsen, C. *Nat. Geosci.* **2008**, *1*, 238–242.
- (31) Omotoso, O.; Mikula, R.; Urquhart, S.; Sulimma, H.; Stephens, P. *Clay Sci.* **2006**, *12*, 88–93.
- (32) Hooshier, A.; Uhlík, P.; Kaminsky, H. W.; Shinbine, A.; Omotoso, O.; Liu, Q.; Ivey, D. G.; Etsell, T. H. *Appl. Clay Sci.* **2010**, *48*, 466–474.
- (33) Eslahpazir, R.; Kupsta, M.; Liu, Q.; Ivey, D. G. *Energy Fuels* **2011**, *25*, 5158–5164.
- (34) Eslahpazir, R.; Liu, Q.; Ivey, D. G. *Characterization of iron-bearing particles in Athabasca oil sands. Energy Fuels* **2012**, *26*, 5036–5047.
- (35) Chia, C. H.; Munroe, P.; Joseph, S. D.; Lin, Y.; Lehmann, J.; Muller, D. A.; Xin, H. L.; Neves, E. *J. Microsc.* **2012**, *245*, 129–139.
- (36) Furukawa, Y. *Org. Geochem.* **2000**, *31*, 735–744.
- (37) Garvie, L. A. J.; Buseck, P. R. *Meteorit. Planet. Sci.* **2007**, *42*, 2111–2117.
- (38) Zborowski, A.; Robertson, G.; Kung, J.; Mercier, P. H. *Lab-scale Solvent Extraction and Solids Agglomeration of Oil Sands. Oil Sands 2014 Conference*; University of Alberta: Edmonton, Alberta, Canada, 2014.
- (39) Patarachao, B.; Mercier, P. H. J.; Kung, J.; Woods, J. R.; Kotlyar, L. S.; Sparks, B. D.; McCracken, T. *Advances in X-ray Analysis* **2010**, *53*, 220–227.

(40) Mercier, P. H. J.; Patarachao, B.; Kung, J.; Dongbao, F.; Kingston, D. M.; Le Page, Y.; Sparks, B. D.; Kotlyar, L. S.; Woods, J. R.; Toll, F.; McCracken, T.; Ng, S.; Kresta, J. Novel mineralogical quantitative phase analysis methodology applied to Canadian oil sands for ore characterization, processability prediction and optimization of froth treatment technologies. *20th General Meeting of International Mineralogical Association*, Budapest, Hungary, Aug. 21–27, 2010; International Mineralogical Association: Bochum, Germany, 2010.

(41) Mercier, P. H. J.; Patarachao, B.; Kingston, D. M.; Tyo, D. D.; Kung, J.; Le Page, Y.; Woods, J. R.; Sparks, B. D.; Kotlyar, L. S.; Toll, F.; Zborowski, A.; Peeples, A.; Robertson, G.; McCracken, T.; Ng, S.; Kresta, J. Novel mineralogical quantitative phase analysis of fines in oil sands. *Oilsands 2011 Conference*, Edmonton, Alberta, Feb. 22–24, 2011; University of Alberta: Edmonton, Alberta, Canada, 2011.

(42) Couillard, M.; Radtke, G.; Botton, G. A. *Philos. Mag.* **2013**, *93*, 1250–1267.

(43) Couillard, M.; Radtke, G.; Knights, A. P.; Botton, G. A. *Phys. Rev. Lett.* **2011**, *107*, 186104.

(44) Williams, D. B.; Carter, C. B. *Transmission Electron Microscopy*; Plenum: New York, 1996.

(45) Strausz, O. P.; Lown, E. M. *The Chemistry of Alberta Oil Sands, Bitumens and Heavy Oils*; Alberta Energy Research Institute: Calgary, Alberta, Canada, 2003; ISBN 0778530965.

(46) *Kerogen: Insoluble Organic Matter from Sedimentary Rocks*; Durand, B., Ed.; Éditions TECHNIP: Paris, France, 1980.

(47) Egerton, R. F. *Electron Energy-Loss Spectroscopy in the Electron Microscope*, 2nd ed.; Plenum: New York, 1996.